Volumetric Surface-guided Graph-based Segmentation of Cardiac Adipose Tissues on Fat-Water MR Images

Faezeh Fallah
Institute of Signal Processing and System Theory
University of Stuttgart
Stuttgart, Germany

Karim Armanious
Institute of Signal Processing and System Theory
University of Stuttgart
Stuttgart, Germany

Bin Yang
Institute of Signal Processing and System Theory
University of Stuttgart
Stuttgart, Germany

Fabian Bamberg
Center for Diagnostic and Therapeutic Radiology
University of Freiburg
Freiburg, Germany

***Abstract*—Different endocrine roles of cardiac adipose tissues motivate the analysis of their volumes and compositions on large cohort image data sets. This, however, demands reliable robust methods for automated segmentations as manual segmentations are tedious costly and unreproducible. Besides the effects of noise and partial volumes, segmentation of these adipose tissues on clinical medical images is challenged by their similar intensities and features and undetectability of their boundaries. In this paper, we present a feature- and prior-based random walker graph that additionally incorporates a diffusion-based susceptible infected recovered model to guide the segmentation by the curvatures of the surface of the segmented cardiac structures. This method is trained and evaluated for segmenting epicardial, pericardial, and perivascular adipose tissues on volumetric fat-water magnetic resonance images. The obtained results demonstrate its utility for large cohort investigation of these adipose compartments and also any other segmentation task on multichannel images.**

***Index Terms*—Random Walker Algorithm, Feature and Prior Learning, Diffusion-based Susceptible Infected Recovered Model, Surface Curvature, Cardiac Adipose Tissues**

I. INTRODUCTION

Epicardial adipose tissue (EpAT) by having a high release and uptake of free fatty acids, serves as an energy source and plays an anti-inflammatory and a thermo-regulatory role for the heart. It also supports coronary arteries mechanically and has an anti-toxic effect. However, its excess can lead to cardiovascular dysfunction and inflammation. In contrast, pericardial adipose tissue (PeAT) is a visceral fat depot and promotes metabolic syndrome and cardiac fibrosis. Cardiac perivascular (PvAT) adipose tissues can also promote coronary artery and abdominal aortic artery calcification [1].

Despite of these findings, the underlying mechanisms and relationships between morphology and composition of these fat compartments and different disorders are not fully understood [1]. To achieve this understanding, images of a large cohort of diverse age, gender, and clinical profile should be processed by reliable robust segmentation methods as manual segmentations are tedious, costly, and subject to human errors.

Magnetic resonance (MR) imaging provides a noninvasive tool to acquire images for these analyzes. However, its slow acquisition process exacerbates artifacts introduced by cardiac and respiratory motions. Also, the limited spatial resolution of clinical MR imaging, noise, and partial volume effects hinder detection of boundaries between those compartments and thus challenges edge-based segmentation methods [2]. Moreover, similar intensities of these adipose tissues imply powerful feature- and prior-based classifier for their segmentation.

Due to these challenges and to the best of our knowledge, no previous method has been designed so far to automatically segment cardiac adipose tissues on clinical MR images. In this paper, we present a method for automatic 3D segmentation of PeAT, EpAT, and PvAT on volumetric fat-water MR images, simply referred to as *fat-water images* hereinafter. A fat-water image involved a volumetric fat and its corresponding volumetric water image. This method used a random walker graph consisting of a spatial (feature-based) and an aspatial (prior-based) sub-graph that additionally incorporated a diffusion-based susceptible infected recovered (SIR) model to guide the segmentation by the curvatures of the nearby surfaces.

II. MATERIALS AND METHODS

A. MR Image Acquisition and Reference Labeling

On a clinical 3 T scanner, thoraxes of 42 asymptomatic obese volunteers (25 men and 17 women) were scanned in axial orientation with an isotropic spatial resolution of 1.8 mm using a 3D spoiled gradient echo sequence. This provided the volumetric magnitude and phase images of 4 bipolar echoes. To avoid motion artifacts, electrocardiography triggering and breath-holding were applied. Then misalignments between even and odd echoes were corrected [3] and a fat-water decomposition [4] was conducted on them to compute the fat-water images. Fig. 1 shows an axial slice of the acquired images and their fat-water decomposition.

On every fat image, reference masks of PeAT, EpAT, and PvAT were manually segmented using the slice-wise tools of Live Wire and Region Growing of Medical Imaging Interaction Toolkit (MITK) [5]. These masks defined voxel-wise reference labels of all the fat-water images. Out of the 42 fat-water images and their voxel-wise reference labels, training and test data sets were made. The training set contained 23

Magnetic resonance images of this work were acquired under the grant BA 4233/4-1 from German Research Foundation (DFG).

Corresponding author email: int87517@stud.uni-stuttgart.de

978-9-0827-9703-9/19/$31.00

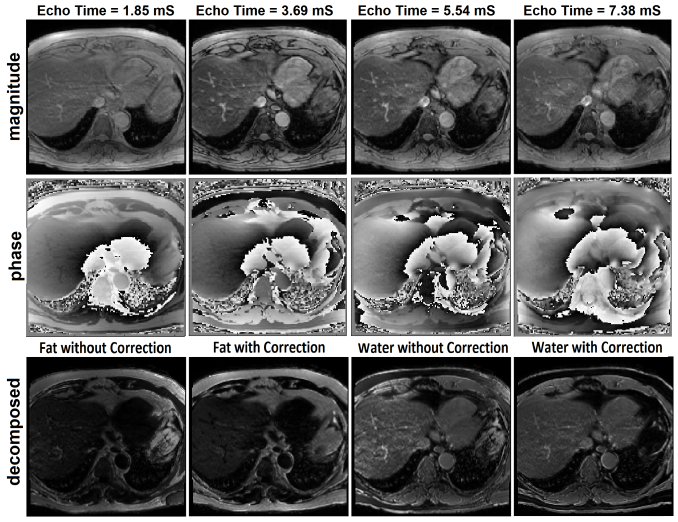

Fig. 1. An axial slice of the acquired magnitude and phase images of 4 bipolar echoes and their decomposed fat and water images with and without correction of misalignments between the odd and even echoes.

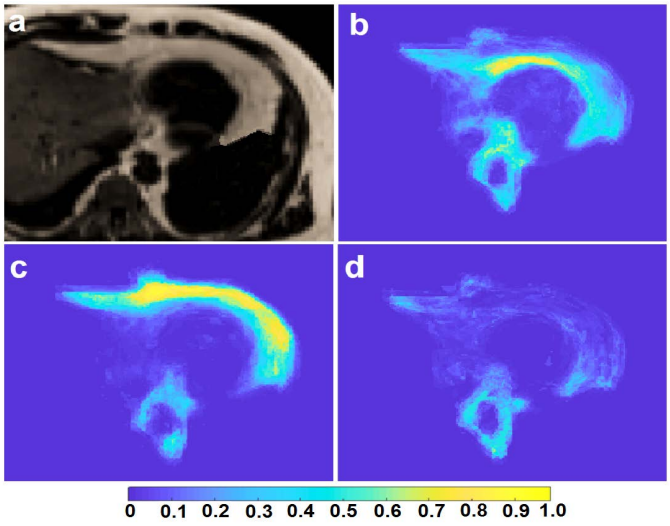

Fig. 2. An axial slice of a test fat image (a), and maps of the priors for EpAT (b), PeAT (c), and PvAT (d) from the random forest classifier.

fat-water images and their voxel-wise reference labels. The test set contained the remaining 19 fat-water images and their voxel-wise reference labels. The training set was used to learn features and priors. The test set was used to evaluate the proposed graph-based segmentation.

B. Training and Test Samples

Every fat-water image was sampled by non-overlapping cubic patches of 27 voxels. From every fat-water patch, 98 features, including 92 intra-channel features and 6 inter-channel features, were extracted. The 92 intra-channel features included 46 fat and 46 water features. The 46 fat/water features included $14 \times 3 = 42$ isotropic (angle-invariant) features of angular mean, range, and standard deviation of 14 Haralick features of a 3D gray-level co-occurrence matrix of 1 voxel displacement in 13 directions [6], average gradient magnitude, average gradient orientation quantized by a regular icosahedron, median of intensities, and the mode of the histogram of gradient (HOG) [7] of intensities. The 6 inter-channel features included fat fraction ratio, fat-water ratio, absolute difference in median of intensities, absolute difference in average gradient magnitudes, l_1 norm of differences in average gradient orientation, and l_1 norm of differences in isotropic Haralick features of a fat and its corresponding water patch. This way, every training sample involved a fat-water patch, its patch-wise reference label (mode of its voxel-wise reference labels), and an 98-dimensional feature vector. Every test sample involved a test fat-water patch and its 98-dimensional feature vector.

C. Feature- and Prior-based Random Walker Graph

According to [8], during the training, the training samples were used to optimize a random forest classifier, over which, the most discriminative features for classifying the test samples were determined. This classifier involved 15 binary decision trees of depth of 4, and, at every decision node, relied on $\sqrt{98} \approx 10$ randomly sampled features of the received training samples. This way, 40 most discriminative features were selected from the 98 features.

During the test, the test samples of every test fat-water image were processed by the trained random forest classifier. This assigned prior probabilities $p_i^{(EpAT)}$, $p_i^{(PeAT)}$, $p_i^{(PvAT)}$, and $p_i^{(BG)}$, corresponding to EpAT, PeAT, PvAT, and background (BG), to every test sample s_i. Then, for the sample s_i, $p_i^{(CaATs)} = p_i^{(EpAT)} + p_i^{(PeAT)} + p_i^{(PvAT)}$ was computed and if $p_i^{(CaATs)} > 0.5$ this sample was labeled as cardiac adipose tissues (CaATs). The prior probabilities and the segmented CaATs were used in the next steps (see subsection II-E). Fig. 2 shows an axial slice of a test fat image and maps of these priors for the three CaATs.

Then, from the test fat-water image inside the bounding box of the segmented CaATs, a random walker graph $G = \{G_s, G_p\}$, involving a spatial (feature-based) $G_s = (V_s, E_s)$ and an aspatial (prior-based) $G_p = (V_s \cup V_p, E_p)$ sub-graph, with vertices V_s and V_p and edges E_s and E_p, was derived.

In the spatial sub-graph G_s, every vertex $v_{s_i} \in V_s$ corresponded to a test sample s_i and the edges were $E_s = \{e_{s_{i,j}} | s_i \text{ is } \textit{adjacent} \text{ to } s_j\}$ with *adjacent* meaning the patches of the test samples being 26-connected neighbors of each other. Weight of an edge $e_{s_{i,j}} \in E_s$ was denoted by $w_{s_{i,j}}$.

In the prior-based sub-graph G_p, every vertex $v_{p_i} \in V_p$ corresponded to a class and was connected to every $v_{s_j} \in V_s$ via an edge $e_{p_{i,j}} \in E_p$. That is, $|V_p| = C$ with C being the number of classes. Weight of an edge $e_{p_{i,j}} \in E_p$ was denoted by $w_{p_{i,j}}$. Fig. 3 shows a portion of these sub-graphs.

Based on [9], edge weights of the prior-based sub-graph G_p were derived from the prior probabilities of the test samples whereas edge weights of the spatial sub-graph G_s were derived from differences in the most discriminative features of adjacent samples. In [9], this graph showed promising results for segmenting tissues of significant feature differences or clear boundaries [9]. However, we observed its limited performance in segmenting cardiac adipose tissues of similar features

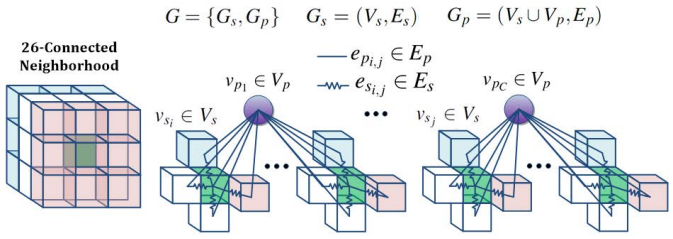

Fig. 3. The 26-connected neighborhood of a voxel and the spatial (feature-based) G_s and aspatial (prior-based) G_p sub-graphs of the image graph.

and undetectable boundaries. To tackle these bottlenecks, we additionally included a diffusion-based SIR model [10] in the spatial sub-graph G_s of the above graph to guide the segmentation by the curvatures of the surfaces of the nearby cardiac structures.

D. The SIR Model

In a random walker graph based on the SIR model [10], the probability of a sample s_i for having the c^{th} class label $1 \leq c \leq C$) was represented by an infection $0 \leq I_{i,t}^{(c)} \leq 1$ incurred to it at time t by its spatially adjacent samples. Similar to [10], we used the steady state solution of this infection diffusion model to determine patch-wise labels (segmentations), i.e. $t \to \infty$ or $t = t_\infty$. This implied no recovery state and a constant (time-independent) susceptibility $0 \leq S_{i,t}^{(c)} = S_i^{(c)} \leq 1$ to the c^{th} infection (class label) for every sample s_i.

However, in contrast to [10], we did *not* assume an identical susceptibility for all the samples. Instead, we *utilized* the susceptibility factor of the original SIR model in order to incorporate additional information into the segmentation. To this end, the SIR model with *sample-dependent* susceptibilities was included in the spatial sub-graph of every test fat-water image. To this end, expanding on a normalized local mean field of the SIR model [10], [11], the evolution of the c^{th} infection of a sample s_i, i.e. $\Delta I_{i,t}^{(c)} = I_{i,(t+\Delta t)}^{(c)} - I_{i,t}^{(c)}$, was determined by its susceptibility $S_i^{(c)}$ and the current infections of its 26-connected (adjacent) samples:

$$\frac{\Delta I_{i,t}^{(c)}}{\Delta t} = \sum_{j \in N_i} \frac{w_{s_{i,j}}}{\sqrt{d_i}} \cdot \left(\frac{S_j^{(c)}}{\sqrt{d_j}} I_{j,t}^{(c)} - \frac{S_i^{(c)}}{\sqrt{d_i}} I_{i,t}^{(c)} \right), \tag{1}$$

where $0 \leq w_{s_{i,j}} \leq 1$ was the weight of the edge connecting $v_{s_i} \in V_s$ and $v_{s_j} \in V_s$; $N_i = \{j | s_j$ is *adjacent* to $s_i\}$ and $d_i = \sum_{j \in N_i} w_{s_{i,j}}$ was the degree of the vertex $v_{s_i} \in V_s$.

By assuming $\Delta t = 1$ and considering $\Delta I_{i,t_\infty}^{(c)} = 0$, the steady state infection $I_{i,t_\infty}^{(c)}$ should fulfill

$$I_{i,t_\infty}^{(c)} = \sum_{j \in N_i} \frac{w_{s_{i,j}}}{\sqrt{d_j} \cdot \sqrt{d_i}} \cdot \frac{S_j^{(c)}}{S_i^{(c)}} \cdot I_{j,t_\infty}^{(c)}, \quad 0 \leq I_{i,t_\infty}^{(c)} \leq 1. \tag{2}$$

Thus the infection of every test sample was a weighted sum of the infections of its adjacent samples. These steady state solutions were obtained by solving a system of C linear equations of a normalized prior-based random walker graph [10], [12]. It is noteworthy that $\sum_c I_{i,t_\infty}^{(c)} \neq 1$. That is, all the C equations should be solved. After solving these equations, the class label of s_i was determined as $\hat{l}_i = \arg\max_c I_{i,t_\infty}^{(c)}$.

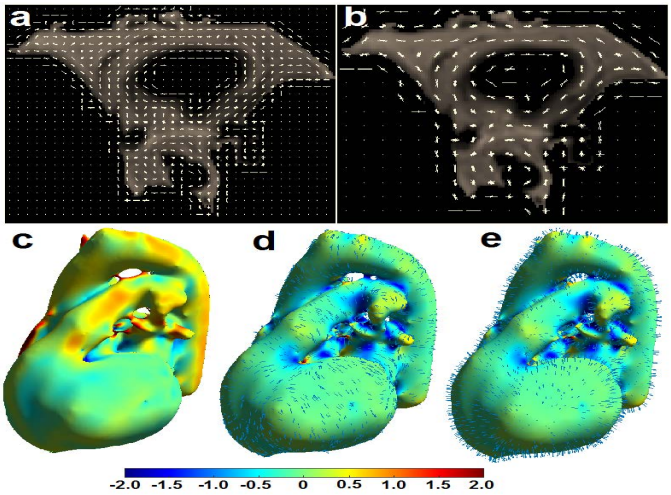

Fig. 4. HOG of intensities of the fat patches of 5^3 (a) and 7^3 (b) voxels on an axial slice of a fat image. Color-coded surface curvatures (c), directions of maximum curvatures over the color-coded Gaussian curvatures (d), and surface normals over the color-coded Gaussian curvatures (e) of the cardiac structures segmented on the corresponding water image. The surface curvatures were clipped to [-2,+2] for a better visualization.

E. The Sample-dependent Susceptibilities

The introduction of the susceptibilities in (2) was motivated by observing that the mode of the HOG of the fat patches belonging to the EpAT were almost aligned with the direction of maximum curvature of the myocardium. Also, the mode of the HOG of the fat patches belonging to the PvAT were almost aligned with the direction of maximum curvature of either of the cardiac vessels. In contrast, modes of the HOG of the fat patches belonging to the PeAT had diverse orientations. Fig. 4 shows these for a segmented cardiac structure and an axial slice of the corresponding fat image. These alignments could be attributed to the synchronous movement of the EpAT with the myocardium during the cardiac motion and the gradual development of the PvAT around vessels.

To utilize these observations, inside the box, bounding the segmented CaATs, an Otsu threshold was applied to the water image to segment cardiac structures including myocardium and cardiac vessels. Surfaces of these segmented volumes were computed, smoothed, and voxelized and their voxel-wise curvatures, normals, and direction of maximum curvatures were computed. Also, the test samples were reduced to the

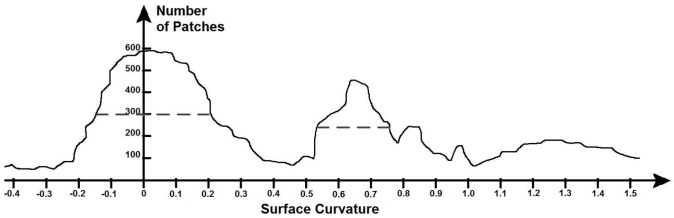

Fig. 5. Histogram of patch-wise average curvatures of a test fat-water image and the FWHM of its main peaks.

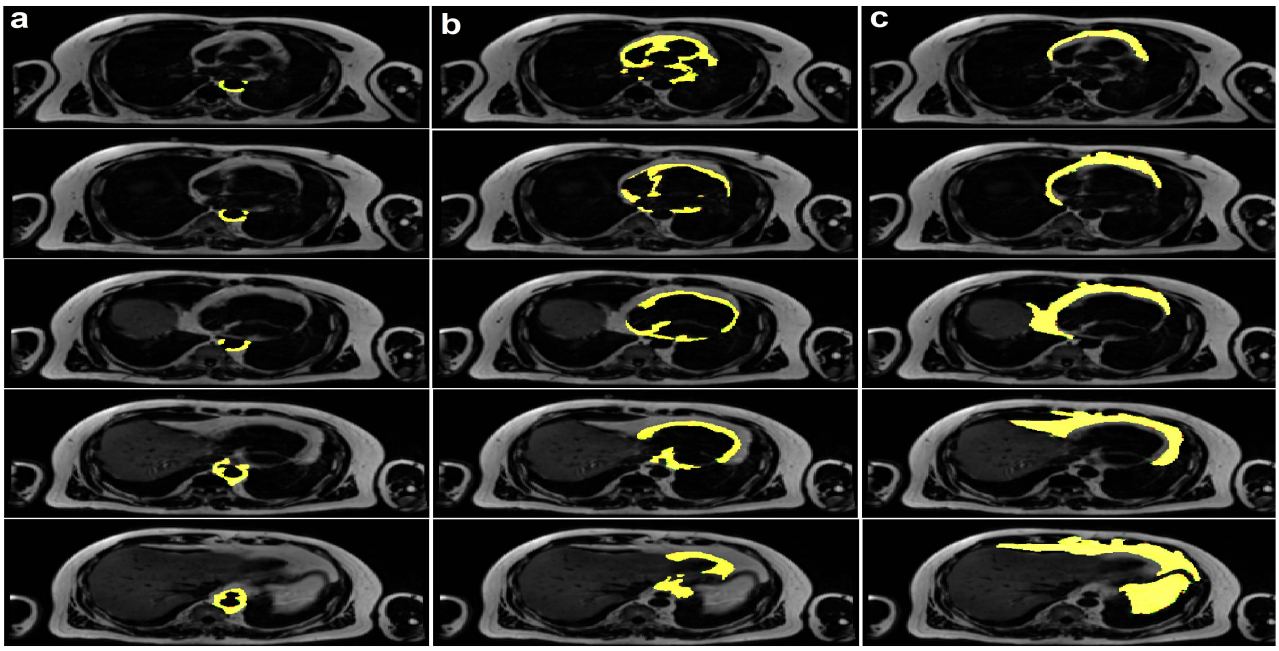

Fig. 6. Axial slices of a test fat image with the reference masks (green), automatically segmented masks (red), and their overlaps (yellow) for PvAT (a), EpAT (b), and PeAT (c).

ones located in the box of the segmented CaATs.

A fat-water patch of a test sample was deemed to be a surface patch if it contained at least one surface voxel. Among all surface voxels of such a patch, average of curvatures, outward normals, and direction of maximum curvatures were calculated. Then, histogram of the patch-wise average curvatures was computed. The lower peak of this histogram was associated to the myocardium and the upper peak to the cardiac vessels. Fig 5 shows this histogram for a test fat-water image. Curvatures inside the full width at half maximum (FWHM) of every peak were considered as the *typical* curvatures of the corresponding cardiac structure. Then, from every surface patch, whose curvature was *typical* for the myocardium, a search was started by following its normal. In each trial of this search, indexed by $u = 1,...,N$, a fat-water patch was hit and the susceptibility of its test sample s_i was defined as

$$S_i^{(c)} = S_i'^{(c)} / (\sum_{k=1}^{4} S_i'^{(k)}), \tag{3a}$$

$$S_i'^{(c)} = \begin{cases} \exp(p_i^{(CaATs)} + d_1) & \text{if } c = \text{EpAT} \\ \exp(p_i^{(CaATs)}) & \text{if } c = \text{PvAT } or \text{ PeAT} \\ \exp(1 - p_i^{(CaATs)}) & \text{if } c = BG \end{cases}, \tag{3b}$$

$$d_1 = k \cdot |\cos(\angle \mathbf{mod}_{HOG_f} - \angle \mathbf{d}_{myo})| / u, \tag{3c}$$

where $k = 4$ was an empirically set factor depending on the size of the image patches; $\mathbf{d}_{myo}$ was the direction of the maximum curvature of the search-starting surface patch of the myocardium and $\mathbf{mod}_{HOG_f}$ was the mode of the HOG of the fat patch of s_i. This way, a sample hit by a lower search trial (u) was more susceptible than a sample hit by a higher trial. Similar search was started from every surface patch, whose curvature was *typical* for the cardiac vessels. The search trials were indexed by $p = 1,...,N$, and the susceptibility of every hit sample s_i was defined as (3) with the difference of

$$S_i'^{(c)} = \begin{cases} \exp(p_i^{(CaATs)}) & \text{if } c = \text{EpAT } or \text{ PeAT} \\ \exp(p_i^{(CaATs)} + d_2) & \text{if } c = \text{PvAT} \\ \exp(1 - p_i^{(CaATs)}) & \text{if } c = BG \end{cases}, \tag{4a}$$

$$d_2 = k \cdot |\cos(\angle \mathbf{mod}_{HOG_f} - \angle \mathbf{d}_{ves})| / p, \tag{4b}$$

and $\mathbf{d}_{ves}$ denoting the direction of the maximum curvature of the search-starting surface patch of the cardiac vessel.

In each trial of the above searches, the susceptibilities assigned to a sample were also assigned to its adjacent samples. This way, every sample could be hit multiple times, either by different search trials or by different neighbors, or not hit at all. If it was hit multiple times, its final susceptibility for every class label was the average of its assigned susceptibilities for that class. If it was not hit at all, its susceptibility was defined as (3) with the difference of

$$S_i'^{(c)} = \begin{cases} \exp(p_i^{(CaATs)}) & \text{if } c = \text{EpAT } or \text{ PvAT } or \text{ PeAT} \\ \exp(1 - p_i^{(CaATs)}) & \text{if } c = BG \end{cases}, \tag{5}$$

F. Evaluation

Masks of the automatically segmented adipose tissues on 19 test fat-water images were evaluated against their reference masks by using the quantitative metrics of dice coefficient (Dice), mean symmetric surface distance (MSSD), and Hausdorff distance (HSD) [9].

III. RESULTS

Fig. 6 shows the automatically segmented masks and the reference masks of cardiac adipose tissues on 5 axial slices

of a test fat image. On 19 test fat-water images, the proposed method achieved dice coefficient (Dice) = 87.4±2.6, mean symmetric surface distance (MSSD) = 1.3±0.25, and Hausdorff distance (HSD) = 4.31±1.34 in the automatically segmented EpAT. Dice = 88.2±1.9, MSSD = 1.1±0.19, and HSD = 4.12±1.28 in the automatically segmented PeAT. Dice = 81.3±2.2, MSSD = 1.61±0.68, and HSD = 5.67±1.52 in the automatically segmented PvAT.

The present method was implemented in C++ and Matlab. On a PC equipped with a quad-core CPU of 3.10 GHz frequency and 16 GB RAM, feature-learning from 23 training fat-water images took 3.5 hours and segmentation of a test fat-water image took 24±7 minutes time.

IV. DISCUSSION

As shown in Fig. 2, an exclusive use of a discriminative feature-learning classifier could not lead to an accurate localization and segmentation of cardiac adipose tissues on fat-water MR images. Clinical cardiac imaging demands breath-holding and electrocardiography triggering to mitigate cardiac and respiratory motions. These imply a fast acquisition and thus a limited spatial resolution that challenges detection of their separating septa, e.g. the visceral pericardium. Additionally, cardiac adipose tissues manifest subtle feature differences which are not enough for their reliable segmentation.

In this paper, we tackled above challenges and proposed a fully automated method for segmenting cardiac adipose tissues on volumetric fat-water MR images. This method expanded on [8]–[10] by incorporating a diffusion-based SIR model into a feature- and prior-based random walker graph in order to additionally guide the segmentation by the curvatures of the segmented cardiac surfaces. This method involved some hyperparameters that were set empirically with respect to the spatial resolution of the recorded images and typical sizes of the cardiac structures.

Contrary to [10], our method relied on a regular image grid and did not consider degree (centrality) of the samples to estimate their labels. This was due to the highly variable distribution of the cardiac adipose tissues in different subjects. Also, we did *not* assume an identical susceptibility for all the samples. Instead, we *utilized* the susceptibility factor of the original SIR model in order to incorporate additional information into the segmentation. Moreover, to avoid misleading effects of undesired feature variations induced by intensity nonuniformities or artifacts, we did not use any clustering method to form our image patches. Finally, by incorporating priors, estimated by a classifier, we provided the random walker seeds automatically and thus mitigated the sensitivity of the random walker algorithm to the number and distribution of these seeds and their errors.

Despite of evaluations on segmenting cardiac adipose tissues, the present method is generic and extendable to other segmentation tasks on any multichannel image. Its computational burden in localizing fat depots can be reduced by incorporating it in a hierarchical segmentation framework [13]. Also, its priors can be estimated by any other classifier such as deep learning methods [14]. However, this method was still challenged by segmenting small fat compartments. Accordingly, it was only trained and evaluated on images of obese subjects. Future extensions of this work could be tackling noise and partial volume effects for a reliable segmentation of small compartments [15] and incorporation of pathological images into the feature- and prior-learning and the SIR model in order to exclude pathologies from fat depots.

The present method is one of the first approaches that tackles fully automated segmentation of cardiac adipose tissues on volumetric fat-water images. Thus, a comparison with the state-of-the-art on the same segmentation task is not possible. Future work would be an application of this method to large cohort data sets and an automated analysis of morphological and pathogenic properties of cardiac adipose tissues in relation to different (sub)clinical disorders.

REFERENCES

[1] P. Iozzo, "Myocardial, perivascular, and epicardial fat," *Diabetes Care*, vol. 34, no. Supplement 2, pp. 371–379, 2011.

[2] F. Fallah, B. Yang, and F. Bamberg, "Automatic atlas-guided constrained random walker algorithm for 3D segmentation of muscles on water magnetic resonance images," in *Proc Eur Signal Process Conf*, 2017, pp. 251–255.

[3] W. Lu, H. Yu, A. Shimakawa, M. Alley, S. B. Reeder, and B. A. Hargreaves, "Water-fat separation with bipolar multiecho sequences," *Magn Reson Med*, vol. 60, no. 1, pp. 198–209, 2008.

[4] D. Hernando, P. Kellman, J. Haldar, and Z. Liang, "Robust water-fat separation in the presence of large field inhomogeneities using a graph cut algorithm," *Magn Reson Med*, vol. 63, no. 1, pp. 79–90, 2010.

[5] I. Wolf, M. Vetter, I. Wegner, T. Böttger, M. Nolden, M. Schöbinger, M. Hastenteufel, T. Kunert, and H. P. Meinzer, "The medical imaging interaction toolkit," *Med Image Anal*, vol. 9, no. 6, pp. 594–604, 2005.

[6] F. Han, H. Wang, G. Zhang, H. Han, B. Song, L. Li, W. Moore, H. Lu, H. Zhao, and Z. Liang, "Texture feature analysis for computer-aided diagnosis on pulmonary nodules," *J Digit Imaging*, vol. 28, no. 1, pp. 99–115, 2015.

[7] W. T. Freeman and M. Roth, "Orientation histograms for hand gesture recognition," MERL - Mitsubishi Electric Research Laboratories, Cambridge, MA 02139, Tech. Rep. TR94–03, 1994.

[8] F. Fallah, B. Yang, S. S. Walter, and F. Bamberg, "A hierarchical ensemble classifier for multilabel segmentation of fat-water MR images," in *Proc Eur Signal Process Conf*, Sep. 2018.

[9] ——, "Hierarchical feature-learning graph-based segmentation of fat-water MR images," in *Proc IEEE Conf Signal Process Algorithms Archit Arrange Appl*, 2018, pp. 37–42.

[10] C. G. Bampis, P. Maragos, and A. C. Bovik, "Graph-driven diffusion and random walk schemes for image segmentation," vol. 26, no. 1, pp. 35–50, 2017.

[11] E. B. Postnikov and I. M. Sokolov, "Continuum description of a contact infection spread in a SIR model," *Math Biosci*, vol. 208, no. 1, pp. 205–215, 2007.

[12] L. Grady, "Multilabel random walker image segmentation using prior models," in *Proc IEEE Comput Soc Conf Comput Vis Pattern Recognit*, 2005, pp. 763–770.

[13] F. Fallah, S. S. Walter, F. Bamberg, and B. Yang, "Simultaneous volumetric segmentation of vertebral bodies and intervertebral discs on fat-water MR images," *IEEE J Biomed Health Inform*, pp. 1–10, 2018.

[14] F. Fallah, D. M. Tsanev, B. Yang, S. Walter, and F. Bamberg, "A novel objective function based on a generalized Kelly criterion for deep learning," in *Proc IEEE Conf Signal Process Algorithms Archit Arrange Appl*, Sept 2017, pp. 84–89.

[15] F. Fallah, J. Machann, P. Martirosian, F. Bamberg, F. Schick, and B. Yang, "Comparison of T1-weighted 2D TSE, 3D SPGR, and two-point 3D Dixon MRI for automated segmentation of visceral adipose tissue at 3 Tesla," *Magn Reson Mater Phy*, vol. 30, no. 2, pp. 139–151, 2017.